Check for updates

ENGINEERING

Biomimetic rigid-soft finger design for highly dexterous and adaptive robotic hands

Ningbin Zhang[1], Peiwei Zhou[1], Xinyu Yang[1], Fengjie Shen[1], Jieji Ren[1], Tengyu Hou[1], Le Dong[1], Rong Bian[1], Dong Wang[1,2], Guoying Gu[1,2]*, Xiangyang Zhu[1,2]*

Copyright © 2025 The Authors, some rights reserved; exclusive licensee American Association for the Advancement of Science. No claim to original U.S. Government Works. Distributed under a Creative Commons Attribution NonCommercial License 4.0 (CC BY-NC).

In dexterous robotic hand design, achieving high mobility and adaptability comparable to human hands remains an ongoing challenge. Biomimetic designs mimicking the musculoskeletal structure have shown promise yet face difficulties in preserving key kinematic and mechanical principles while reducing system complexity. Here, we present a biomimetic finger design that preserves these principles through coordinated rigid-soft interplay, achieving structural and control simplicity for constructing dexterous robotic hands. Our design distills complex anatomical structures into skeletal mechanisms with regular geometrics, strategically deployed soft ligaments, and elastic tendon actuation, enabling controllable multi–degree-of-freedom dexterity while providing resilience and compliance. We establish mathematical models to analyze finger kinematics, rigid-soft interplay principles, and controllable actuation. Building on these models, we integrate biomimetic fingers with a thumb to develop an anthropomorphic robotic hand. Our robotic hand experimentally demonstrates remarkable dexterity and versatility across various tasks, including piano playing, power and pinch grasping, and in-hand manipulation, confirming the design effectiveness.

INTRODUCTION

Designing robotic hands to replicate the embodied dexterity of human hands has been a long-term pursuit in robotics, aiming to achieve both active high mobility and passive adaptivity. This pursuit poses critical challenges, as designers must balance multiple functionality factors including degrees of freedom (df), kinematics, interactive contact, and system cost (*1*). The traditional approach primarily addresses active high mobility, using exquisite rigid-material mechanisms to implement controllable multi-df mobilities within a limited compact space (*2*–*4*). However, the inherent rigid constraints imposed by these mechanisms often increase the complexity of design, fabrication, and control, potentially limiting the adaptivity of robotic hands.

To overcome the adaptivity limitation, soft robotics (*5*–*11*) has emerged as a promising solution. By using low modulus materials to build compliant mechanisms, soft robotic hands achieve inherent adaptivity with continuous conformable deformation (*12*–*21*). This inherent adaptivity endows robotic hands with remarkable advantages, including high flexibility and resilience (*12*, *13*, *22*–*24*), reduced structural and control complexity (*14*, *18*, *25*, *26*), and compliant safe interactions (*17*, *18*, *24*). Despite these advantages, the soft approach faces challenges in achieving controllable active high mobility, a key strength of rigid-material designs. These challenges stem from the inherent properties of soft materials, including low force output, nonlinear mechanics, and slow response times (*27*).

In parallel to soft robotic development, efforts have been made to explore a rigid-soft hybrid approach inspired by the human hand's musculoskeletal system (*28*–*32*). This approach integrates components with varied moduli to emulate bones, muscles, ligaments, and tendons and has been facilitated by advances in multimaterial three-dimensional (3D) fabrication technologies (*31*, *33*). Because of the interplay of rigidity and flexibility, these hybrid structures have proven to enable human-like configurations (*28*, *29*, *34*), variable force output (*30*, *35*, *36*), compliant interactions (*37*), and autonomous force-velocity adaptation (*38*). This hybrid approach has shown promising results in dexterous manipulation. For instance, Hughes *et al.* (*39*) have demonstrated that a biomimetic soft skeleton hand can perform various piano playing styles passively, presenting a stark contrast to robotic hands that rely purely on actively controlled mobility (*40*–*45*). This difference in performance can be attributed to the passive adaptivity of the soft skeleton hand and the active external dexterity of a robotic arm connected to the hand.

However, achieving embodied dexterity in a rigid-soft hybrid approach still presents significant challenges. The primary challenge lies in creating rigid-soft coordinated engineered systems that mimic biological structures while combining multi-df mobility and adaptive interaction. Most previous designs directly replicate biological structures such as irregular skeleton shapes (*28*, *34*), nonlinear variations in ligament tension (*30*, *32*), and intricate tendon/muscle mechanisms (*30*, *31*). While biomimetic, this approach often hinders the realization of well-defined kinematics and multi-df control. On the other hand, achieving adaptivity poses challenges in effectively coordinating rigid and soft components, especially within a single robotic hand system driven by multiple actuation channels. Consequently, these robotic hands typically lack sufficient built-in actuation channels or resort to external dexterity (*37*, *39*). These challenges underscore the importance of balancing complex rigid-soft interactions in multijoint mechanics, actuation mechanisms, and corresponding algorithms to achieve embodied dexterity and adaptability (*2*).

Here, we present a coordinated rigid-soft approach for designing biomimetic fingers, combining controllable high mobility with adaptivity while preserving the human finger's key kinematic and mechanical principles (Fig. 1A and movie S1). In this approach, we integrate regular-shaped skeletons with strategically placed soft ligaments to form multimaterial joints (Fig. 1B), complemented by compact elastic tendon actuation for controlled multi-df movements and

[1]Robotics Institute and State Key Laboratory of Mechanical System and Vibration, School of Mechanical Engineering, Shanghai Jiao Tong University, Shanghai 200240, China. [2]Shanghai Key Laboratory of Intelligent Robotics, Meta Robotics Institute, Shanghai Jiao Tong University, Shanghai 200240, China.
*Corresponding author. Email: guguoying@sjtu.edu.cn (G.G.); mexyzhu@sjtu.edu.cn (X.Z.)

Downloaded from https://www.science.org at Shanghai Jiao Tong University on April 28, 2025

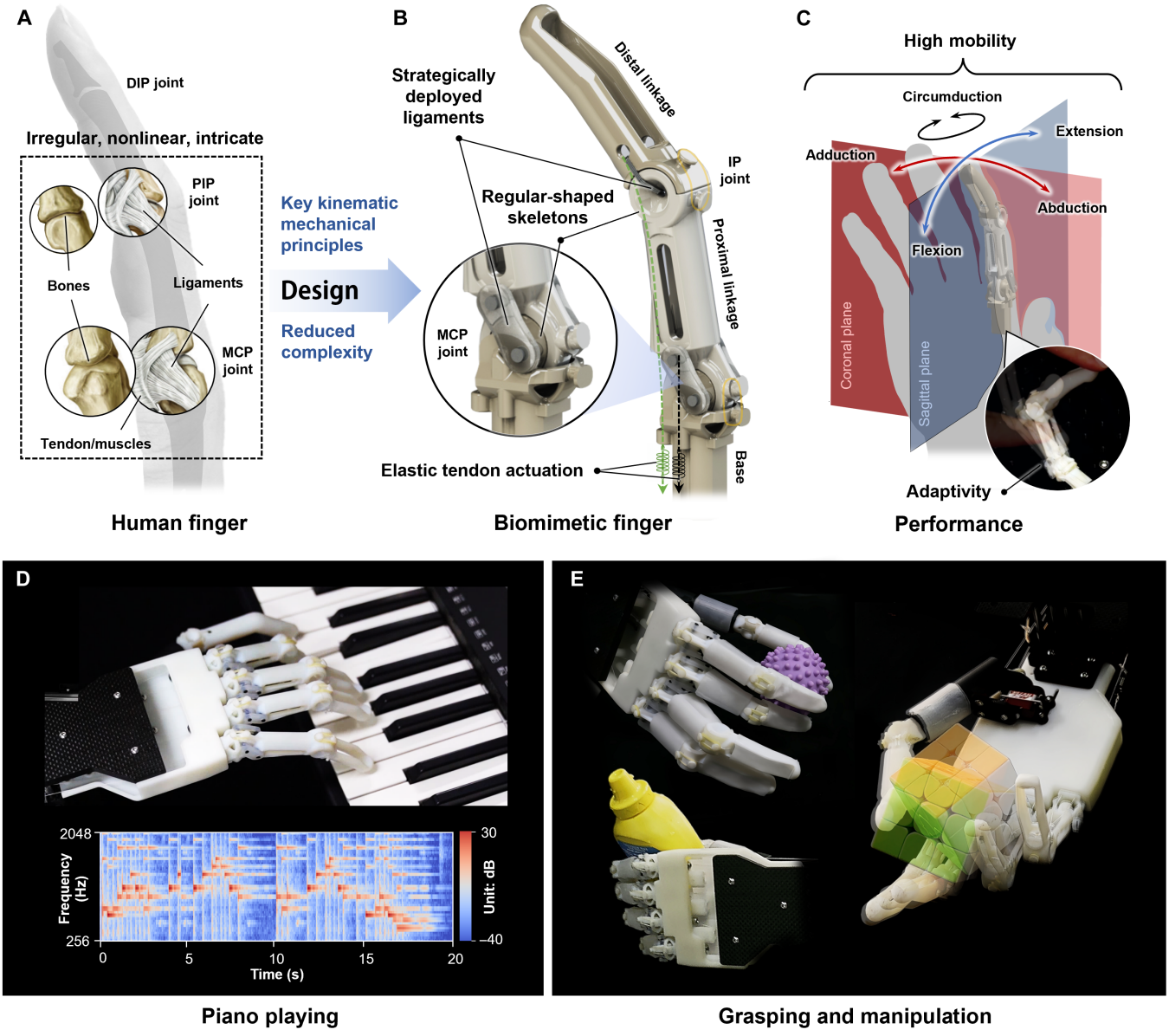

Fig. 1. Design concepts, working principles, and applications of the biomimetic finger. (**A**) The complex musculoskeletal and ligamentous structures of the human finger. PIP, proximal interphalangeal; DIP, distal interphalangeal. (**B**) A holistic design of the biomimetic rigid-soft finger with reduced complexity. The finger features regular-shaped skeletal mechanisms, strategically deployed ligaments, and elastic tendon actuation. (**C**) Working principle of the biomimetic finger with multiple joints to achieve multi-df mobility and adaptive interaction. (**D**) Demonstration of an anthropomorphic robotic hand integrating the biomimetic fingers and a thumb mechanism for dexterous manipulation. Through coordinated multifinger control, the anthropomorphic robotic hand can perform piano music with a human-like behavior (top). The spectral analysis shows the accuracy of the played music (bottom). (**E**) Demonstration of the anthropomorphic robotic hand performing general grasping and in-hand manipulation.

compliance (Fig. 1C). These components are easy to model and fabricate, facilitating their integration into an anthropomorphic robotic hand with coordinated multifinger control. We evaluate the robotic hand's performance through a series of piano playing tasks (Fig. 1D) and general tasks from grasping to manipulation (Fig. 1E). The results demonstrate the significant potential of biomimetic rigid-soft design for highly dexterous and adaptive robotic hands.

RESULTS

Rigid-soft hybrid design of the biomimetic finger

Inspired by the human finger anatomy, we designed the biomimetic finger, incorporating three essential components: skeletons, ligaments, and actuation mechanisms. The skeletal structure consists of a base, a proximal linkage, and a distal linkage. Adopting human finger anatomical nomenclature (*46*), the proximal linkage connects

Downloaded from https://www.science.org at Shanghai Jiao Tong University on April 28, 2025

to the base via a metacarpophalangeal (MCP) joint, and the distal linkage connects to the proximal linkage through an interphalangeal (IP) joint. Kinematically, the MCP joint primarily enables flexion-extension (rotation angle θ) and abduction-adduction (rotation angle φ), along with limited circumduction (Fig. 2A). The IP joint, in contrast, allows only flexion-extension (rotation angle ζ). Using the joint parameter set (θ, φ, and ζ) and linkage dimensions, we can establish a clear kinematic model for finger configuration control (detailed in fig. S1 and text S1). Mechanically, the MCP joint exhibits variable stability due to the variation of ligament tension, enabling adaptive environmental interaction and stabilization of the loose joint motion caused by skeleton-to-skeleton contact. The IP joint, with its ligaments effectively constraining unwanted off-axis motions throughout the entire range of motion, acts similarly to a typical revolute joint to enhance finger stability.

We use tendon actuation for the biomimetic finger due to its high efficiency and compactness. A tendon passes through both the MCP and IP joints for underactuated flexion, mimicking the human deep flexor tendon (*46*). Elastic extensors on the back of the joints enable joint extension with the release of the tendon. Another tendon passes through the MCP joint for its abduction, and the elastic ligament enables joint adduction with the release of the tendon. Springs are integrated with both the tendon pathways, which maintain joint compliance and emulate the resilience of biological counterparts. The tendons are connected to actuators (e.g., motors with pulleys) to generate controlled joint movements, allowing precise modulation of tendon displacement (detailed in fig. S2 and text S2). With this design concept, we aim to explore an effective approach to replicate a rigid-soft hybrid system, capturing the essence of human finger kinematics and mechanics.

The MCP joint plays a crucial role in finger function, making it a focal point of our design. It incorporates a ball-ring pair with elliptical blocks (BRE mechanism), complemented by lateral elastic ligaments (Fig. 2B). In the BRE mechanism, the ring loosely encircles the ball with a submillimeter-scale clearance to perform rotational motions of flexion-extension, abduction-adduction, and circumduction. The elliptical blocks serve a vital function by constraining the ring motion within a confined workspace similar to that of the human finger. As the ring moves from the fully extended position (θ = 0°) to its fully flexed position (θ = 90°), the abduction range gradually decreases. This decrease is due to the narrowing gap between the elliptical block's edge and the ring's edge, mirroring the skeletal constraints of the human MCP joint surfaces (fig. S3A). To replicate the kinematics of the human MCP joint, we develop a theoretical model to analyze the influence of the dimensional parameters of the BRE mechanism on its workspace (Fig. 2C). In this model, there are four key parameters: ball radius (R), long axis of the elliptical block (a), its short axis (b), and the distance between the linkage end and the ball center (H). Using a coordinate system O-xyz, we denote flexion as the ring's rotation angle θ around the z axis and abduction as the rotation angle φ around the x axis. The elliptical block's edge is formulated as curve $C_e = x^2/a^2 + y^2/b^2 = 1$. The projection of the ring's edge is represented by line $l_e = y\cos\theta = -x\sin\theta + h$, where h is the distance between line l_e and the ball center. The ring's motion can be described as a combination of an abduction angle φ following a flexion angle θ, with φ increasing from 0° until the ring's edge contacts the block's edge. During this process, distance h decreases until line l_e contacts curve C_e. The corresponding maximum abduction angle can be calculated by $\varphi_{max}(\theta) = \pi/2 - \arccos H_R - \arcsin\sqrt{a_R^2\sin^2\theta + b_R^2\cos^2\theta}$, where $a_R = a/R$, $b_R = b/R$, and $H_R = H/R$ are all dimensionless parameters (detailed in text S3). Therefore, angle $\varphi_{max}(\theta)$ is determined by design parameters $\{a_R, b_R, H_R\}$, and the 3D workspace is enveloped by $\theta \in [0, \pi/2]$ and $\varphi \in [-\varphi_{max}(\theta), \varphi_{max}(\theta)]$. From a design perspective, we can determine the design parameters $\{a_R, b_R, H_R\}$ by solving three equations based on the given conditions $\{\varphi_{max}(\theta_1), \varphi_{max}(\theta_2), \varphi_{max}(\theta_3)\}$. For engineering simplicity, the parameter H_R is set to a constant H_{R0}. In this sense, we can derive the design parameters $\{a_R, b_R\}$ with a given $\{\varphi_{max}(\theta_1), \varphi_{max}(\theta_2)\}$ for the BRE mechanism

$$\sqrt{a_R^2\sin^2\theta_i + b_R^2\cos^2\theta_i} = \sin\left[H_{R0} - \varphi_{max}(\theta_i)\right],\ (i = 1, 2) \quad (1)$$

On the basis of the theoretical model, we can conduct a parametric design for the desired workspace (Fig. 2D). Theoretical and measured experimental results show good agreement across all parameter sets. The detailed experimental setups and calculations for the workspace measurement are provided in fig. S4 and text S4. The slight differences between theoretical and experimental results show a mean absolute deviation of 4.2°, 3.9°, and 2.8° in the x-y plane, x-z plane, and z-y plane, respectively (fig. S5). These differences likely stem from the ball-ring clearance and measurement errors. We choose the parameter set $\{a_R = 0.87, b_R = 0.5\}$ to form a workspace boundary $\{\varphi_{max}(0°) = 30°, \varphi_{max}(90°) = 0°\}$ similar to the human MCP joint (*46*). In addition to the primary motions of flexion-extension (rotation around the z axis) and abduction-adduction (rotation around the x axis), the BRE mechanism allows limited circumduction motion around the y axis without adding extra structural complexity (detailed in fig. S6). This feature enables the joint to adapt its movement in response to unexpected payload from any direction, which distinguishes it from existing designs that use rigid two-df universal joints (*47*–*49*) and condyloid joints (*50*) or resort to complex multilinkage-coupled designs (*4*) to replicate the kinematics of the human MCP joint. Besides, the ball-ring clearance in our design is set as 0.2 mm, considering the operation stability, manufacturability, and durability of the BRE mechanism (detailed in text S5 and fig. S7).

On the other hand, elastic ligaments serve to stabilize the joint and provide compliant resilience. We achieve this by attaching them to the BRE mechanism with offset anchoring points, mimicking the cam effect principle (*46*, *51*, *52*) of the lateral ligaments in the human MCP joint (fig. S3B). We establish a theoretical model to analyze the effectiveness of the design (Fig. 2E). The proximal anchor P is located on the elliptical block with length $l_{OP} = \xi R$, and the distal anchor Q is located on the midline of the linkage with length $l_{OQ} = \lambda R$. The parameters (ξ, $\xi < a_R < 1$) and (λ, $\lambda > 1$) are scale factors. According to the theoretical model (detailed in text S5), we can obtain the variation of the ligament tension when the BRE mechanism executes flexion

$$\Delta T(\theta) = \Delta l(\theta) k_E = \left(\sqrt{\xi^2 + \lambda^2 + 2\xi\lambda\sin\theta} - \sqrt{\xi^2 + \lambda^2}\right) R k_E \quad (2)$$

where $\Delta l(\theta)$ is the ligament stretch at flexion angle θ and k_E is the elastic modulus of the ligament material. The finite element simulation (Fig. 2F and fig. S8) indicates that the ligament's maximum strain is 94.6%, where the parameter k_E is approximately regarded as constant for simplicity. Thus, the tension variation $\Delta T(\theta)$ is a monotonic increasing function for $\theta \in [0, \pi/2]$. The increasing tension variation helps stabilize the loose BRE mechanism and provides the

Downloaded from https://www.science.org at Shanghai Jiao Tong University on April 28, 2025

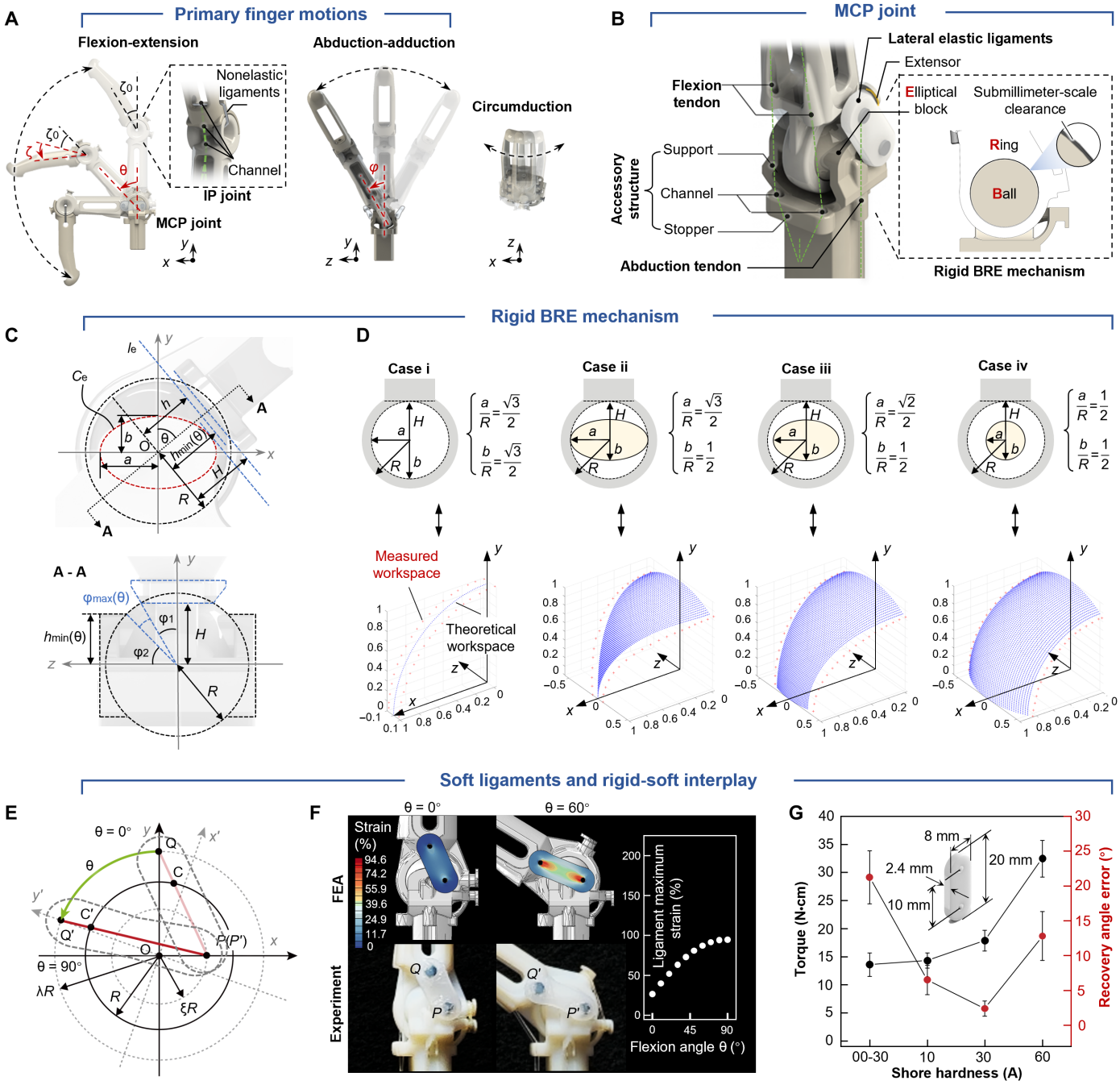

Fig. 2. Mechanical design and structural analyses. (**A**) The mobility of the multijoint biomimetic finger. Finger flexion-extension is achieved by the underactuated MCP joint (angle θ) and IP joint (angle ζ), abduction-adduction is achieved by the MCP joint (angle φ), and circumduction is passively obtained on the MCP joint. ζ_0, IP joint's initial flexion angle. (**B**) Rigid-soft hybrid structure of the MCP joint. This joint consists of a rigid BRE mechanism, a pair of lateral elastic ligaments, flexion/abduction tendons, and accessory structures. (**C**) Kinematic modeling of the BRE mechanism. C_e, edge function of the elliptical block; l_e, edge function of the linkage's end plate; *R*, ball's radius; *a*, elliptical block's long axis length; *b*, elliptical block's short axis length; *H*, distance from the linkage's end plate to the ball center; *h*, distance from line l_e to the ball center; $h_{min}(\theta)$,minimum *h* for a given θ; $\varphi_{max}(\theta)$, maximum φ for a given θ. (**D**) Parametric workspace design of the BRE mechanism under varied structural parameters (a_R and b_R). The theoretical workspace exhibits good shape agreement with the experimental results in all cases. (**E**) Modeling of the elastic ligament's stretch upon flexion. Light red, ligament length at θ = 0°; dark red. ligament length when θ > 0°. (**F**) Finite element analysis (FEA) of the ligament strain during its stretching. The maximum strain is 94.6% at θ = 90°. (**G**) Ligament material selection is based on the recovery angle error and required actuation torque. We selected the material with 30A hardness because ligaments made from it exhibit the smallest recovery angle error while requiring only moderate actuation torque.

Downloaded from https://www.science.org at Shanghai Jiao Tong University on April 28, 2025

mechanism with resilience to the initial joint position. We select the ligament material through an experimental method (fig. S9). Among material candidates with varied hardness, the 30A-hardness silicone (Young's modulus under 100% strain, $k_E = 593$ kPa) is selected because it offers sufficient resilience ($n = 20$ trials, average 2.3° recovery angle error) to bring the joint to the initial position while maintaining an acceptable level of actuation torque consumption (Fig. 2G). The soft ligaments and rigid BRE mechanism engage in a bioinspired, coordinated interplay. The soft ligaments provide enhanced stability and compliant resilience to the BRE mechanism, while the BRE mechanism's rigid geometrical constraints protect the ligaments from overstretching. This stands in contrast to typical soft joint/finger designs (*12*–*18*), which typically compromise stability for flexibility.

Performance characterization of the biomimetic finger

Next, we use high-resolution PolyJet 3D printing (J750 printer, Stratasys Ltd.; *x/y/z* resolution, 42/42/14 μm) and soft molding (*6*) to fabricate finger prototypes with varied moduli and sophisticated structures (detailed in Materials and Methods). The parameters of these structures are shown in table S1. On the fabricated finger prototypes, we experimentally characterize a series of finger performances, where the spring-attached tendons for flexion (termed f-tendon) and abduction (termed a-tendon) are connected to the pulleys on servomotors in position control mode (i.e., the servomotor output is the desired rotation angle). Details on the relationships between the servomotor rotation angle, tendon and spring displacement, and speed are illustrated in Materials and Methods. Upon tendon actuation, the finger can perform active motions of flexion-extension and abduction-adduction (Fig. 3A). The maximum finger speeds are 106.3° and 88.5°/s for the flexion-extension cycle and abduction-adduction cycle, respectively. The elastic components (i.e., ligaments, springs, and extensors) provide the finger with resilience for the above movements and recoverable circumduction under external force (Fig. 3B).

To investigate the applied force when the finger touches an object, we next characterize the influence of f-tendon displacement ($\Delta L_{flexion}$) on the finger output force (Fig. 3C). The finger is initially tendon actuated to different flexion angles (denoted as $\theta_{initial}$), with its fingertip touching the force sensor with no load. Then, the finger is continually actuated to generate increasing fingertip force, which is denoted as $f_{flexion}$, and measured for $n = 3$ trials. Results demonstrate that force $f_{flexion}$ generally increases with displacement $\Delta L_{flexion}$ through the transmission of elongated spring connected to the tendon but is not positively correlated with $\theta_{initial}$ (Fig. 3D). The minimal displacement for generating enough force ($f_{flexion} = 0.55$ N; fig. S10) to play the piano keyboard is $\Delta L_{flexion} = 2.0$ mm at $\theta_{initial} = 0°$. The finger stiffness is 25 ± 1.1 and 21 ± 2.7 N/m in the flexion-extension direction and flexion-extension direction, respectively (see fig. S11 for detailed experimental setups). Long-term cycling tests reveal the stability of force $f_{flexion}$, with a 6.44% degradation over 1000 loading-unloading cycles (Fig. 3E). For the relationship between the a-tendon displacement $\Delta L_{abduction}$ and fingertip force $f_{abduction}$ (Fig. 3F), we find that force $f_{abduction}$ has a positive relationship with $\theta_{initial}$ (Fig. 3G). Long-term cycling tests also confirm the stability of force $f_{abduction}$, with a 9.56% degradation over 1000 loading-unloading cycles (Fig. 3H). These small performance degradations can be attributed to slight tendon relaxation in the actuation system, material fatigue from repeated loading-unloading cycles, and a small amount of friction wear in the ball-ring clearance. Methods such as implementing durable tendon-tensioning mechanism designs (*53*), using tough printable materials (*33*), and optimizing lubrication (*34*) may further enhance the durability of the finger mechanism. For the dynamic properties, the biomimetic finger achieves response times of 220 ms (flexion-extension) and 170 ms (abduction-adduction). The bandwidths are about 1.25 and 3.70 Hz for the flexion-extension and abduction-adduction motions, respectively (detailed in Materials and Methods and fig. S12). The above dynamic performance is generally comparable to the requirements of daily activities performed by the human hand (*46*).

Development of an anthropomorphic robotic hand

To exploit the application potential of our proposed finger design, we develop an anthropomorphic robotic hand that integrates four fingers and an opposable thumb (Fig. 4A). The opposable thumb consists of two key joints: a carpometacarpal (CMC) joint and a thumb-MCP (TMCP) joint. The CMC joint uses a direct drive mechanism using a servomotor to achieve thumb opposition. Its motion range is calibrated, with a partial stroke (about 0° to 45°) serving as the flexion motion. The TMCP joint uses a tendon actuation and is designed to perform abduction-adduction, further enhancing the thumb's dexterity and ability to perform complex manipulations. The detailed mechanical structures of these joints are illustrated in fig. S13.

The anthropomorphic robotic hand has eight independent actuation inputs. The thumb is actuated by a CMC joint servomotor and a TMCP joint tendon. The index and little fingers are each actuated by two tendons for active MCP-IP joint flexion and MCP joint abduction, respectively. The middle and ring fingers are each actuated by a single tendon for active MCP-IP joint flexion, while the abduction tendon is eliminated for simplification. Except for the CMC joint, the other joints are driven by seven actuation modules, each integrating a servomotor, tendons, springs, and pulleys (fig. S14). A control module comprises a microcontroller unit board and a servo driver that enables multichannel precise control. All components are assembled within the palm and forearm of the robotic hand (fig. S15).

Piano playing skill evaluations

Piano playing represents an excellent benchmark for evaluating the performance of robotic hands (*39*–*45*) due to its complex requirements for controllable active high mobility (e.g., performing scales and chords), adaptive interaction (e.g., performing glissandos), and different sound levels for the same note. To address these challenges, we use our developed anthropomorphic robotic hand, mounted on a single-axis moving platform, to perform these tasks (Fig. 4, B and C, and movie S2). Detailed experimental setups are provided in Materials and Methods.

The scale-playing task is used to evaluate the robotic hand's ability to cover a wide range of notes without resorting to unnatural whole-hand movements. Figure 4D shows that the robotic hand can span at most 10 notes, with each finger accurately pressing the corresponding key ($n = 5$ repetitions). This performance is primarily attributed to the active abduction ability of fingers. Specifically, the index and little fingers each have three configurations (termed I1, I2, and I3 and L1, L2, and L3, respectively), while the thumb can produce three configurations through its TMCP joint (termed T1, T2, and T3). Thumb opposition, achieved through combined rotations of the TMCP and CMC joints, plays a critical role in dexterous

Downloaded from https://www.science.org at Shanghai Jiao Tong University on April 28, 2025

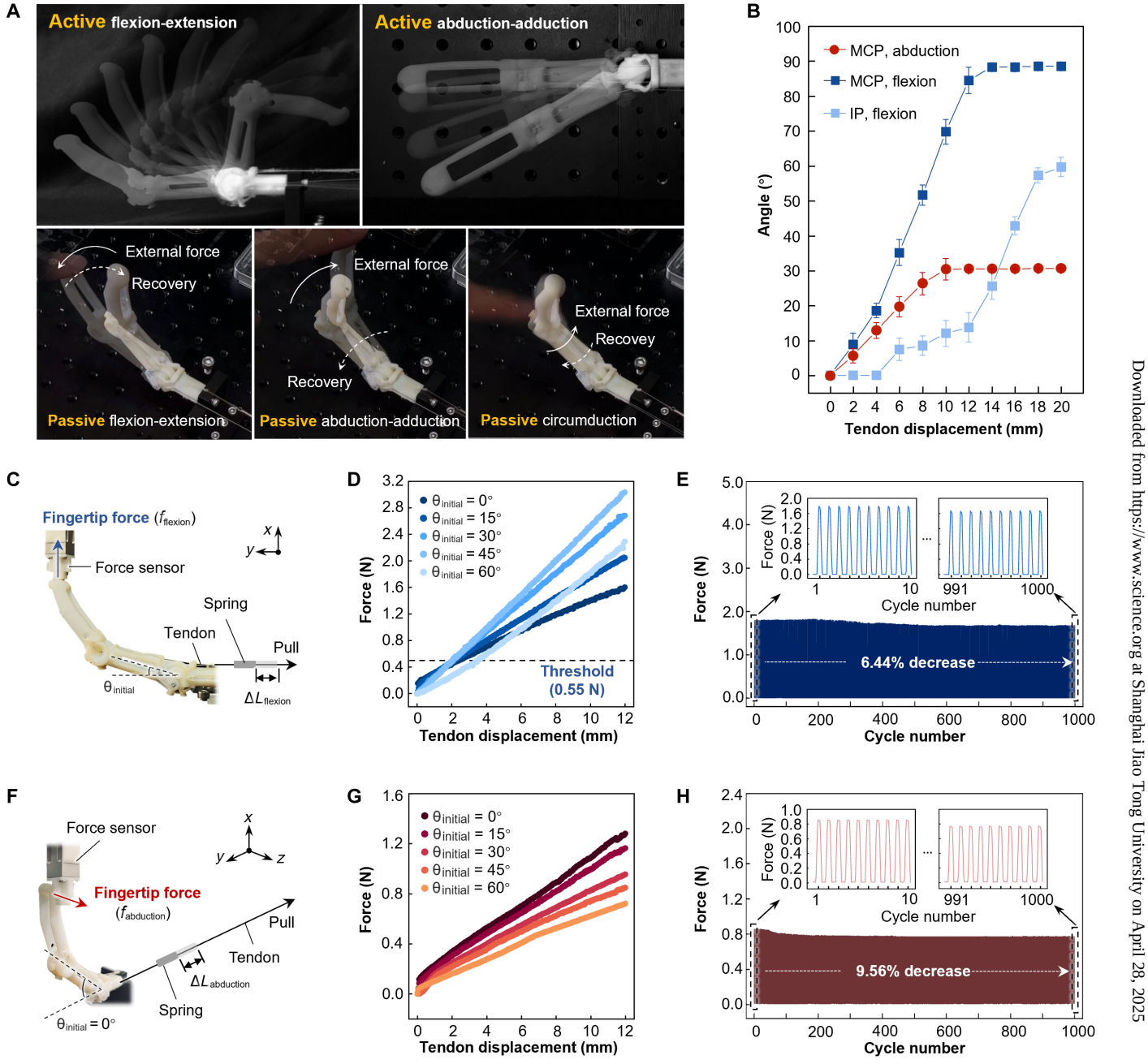

Fig. 3. Kinematic and mechanical performance characterization. (**A**) Active and passive finger movements. Upon tendon actuation, the biomimetic finger executes flexion-extension and abduction-adduction (top). It also exhibits passive motions under external force (bottom). (**B**) The relationships between tendon displacements and corresponding joint angles. (**C**) Experimental setups for measuring the fingertip force $f_{flexion}$. $\Delta L_{flexion}$, tendon displacement for flexion. (**D**) Variations of fingertip force $f_{flexion}$ with different tendon displacements $\Delta L_{flexion}$ and initial flexion angles $\theta_{initial}$. (**E**) Stability of fingertip force $f_{flexion}$ during 1000-cycle flexion-extension. The insets show the first and last 10 cycles. (**F**) Experimental setups for measuring the fingertip force $f_{abduction}$. $\Delta L_{abduction}$, tendon displacement for abduction. (**G**) Variations of fingertip force $f_{abduction}$ with different tendon displacements $\Delta L_{abduction}$ and initial flexion angles $\theta_{initial}$. (**H**) Stability of fingertip force $f_{abduction}$ during 1000-cycle abduction-adduction. The insets show the first and last 10 cycles.

manipulation tasks, where the TMCP joint allows the thumb to select among three adjacent piano keys and the CMC joint enables it to press the selected key (see movie S3 and fig. S16). These results demonstrate the robotic hand's ability to produce active dexterous movements akin to the human hand, exhibiting consistent repeatability and reliable execution speed.

The glissando-playing task, which involves rapid successive transitions between notes, is used to evaluate the robotic hand's ability to adaptively interact with the piano. This is particularly useful in conveying emotions, as exemplified in the famous music piece "Rhapsody in blue" (*39*). Figure 4E shows that with only active uniaxial translation (speed of 210 mm/s) of the arm moving platform, the

Downloaded from https://www.science.org at Shanghai Jiao Tong University on April 28, 2025

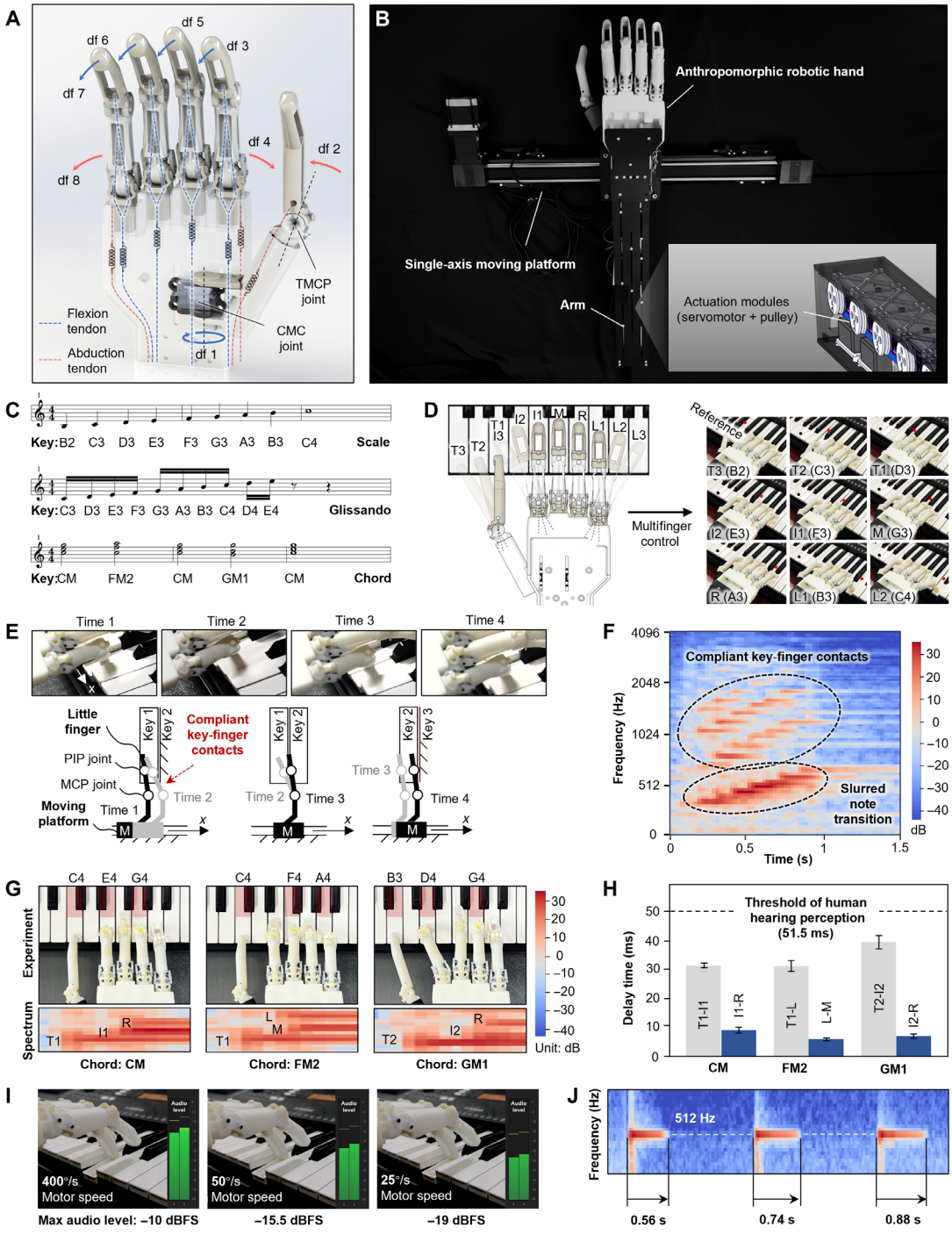

Fig. 4. Development of an anthropomorphic robotic hand and its piano playing skills. (**A**) Structure of the anthropomorphic robotic hand with four fingers and an opposable thumb. The robotic hand has a total of eight independent control inputs. (**B**) Demonstration of the robotic hand system mounted on a single-axis moving platform for piano playing. (**C**) Illustration of three selected piano playing skills including the scale, glissando, and chord. (**D**) Demonstration of the robotic hand performing a scale. It can play up to 10 distinct notes with different finger poses (left). T1 to T3, thumb poses; I1 to I3, index finger poses; M, middle finger pose; R, ring finger pose; L1 to L3, little finger poses. A nine-note scale is performed for musical conventions (right). (**E**) Demonstration of the robotic hand performing a glissando. In this process, the finger adaptively interacts with the keyboard. (**F**) The spectral analysis reveals the smooth note transitions and the compliant finger-keyboard interactions. (**G**) Demonstration of the robotic hand performing chords. In this process, multiple notes are played almost simultaneously. (**H**) In this process, the delay time between notes is less than the minimum interval perceivable by the human ear (*53*). (**I**) Demonstration of the robotic hand producing different sound levels for the same note. The finger is actuated at motor speeds of 400°, 50°, and 25°/s to press the piano key, resulting in maximum audio levels of −10, −15, and −19 dBFS (decibels relative to full scale), respectively. (**J**) The spectral analysis reveals that the three sounds produced are not distorted by the different motor speeds, with all frequencies centered around 512 Hz. The higher the motor speed, the shorter the time required to generate the sound.

Downloaded from https://www.science.org at Shanghai Jiao Tong University on April 28, 2025

little finger slides over a series of piano keys, exhibiting passive abduction-adduction to interact with the piano keys smoothly and repetitively ($n = 5$ repetitions). This performance can be explained by a schematic model, which attributes this behavior primarily to the passive compliance and elasticity of the MCP joint, allowing it to quickly conform to variations in the touched surface conditions. Mel spectral analysis further confirms that the produced sounds are soft and slurred, accompanied by the subtle sounds of repetitive compliant finger-key interactions (Fig. 4F).

The chord-playing task is used to evaluate the robotic hand's ability to simultaneously play multiple notes (Fig. 4G). We select a musical piece featuring several three-note chords (designated as CM, FM2, and GM1). During the execution of CM and FM2 chords, all fingers and the thumb maintain their initial positions. For the GM1 chord, while the ring finger remains in its initial position, the thumb and index fingers abduct by one note ($n = 5$ repetitions). Experimental results show that the robotic hand can precisely coordinate multiple notes in different chords and switch rapidly between them. The spectral analysis further reveals that the produced chords have low internote delays (Fig. 4H), which fall below the threshold of human auditory perception (*54*).

The robotic hand demonstrates the ability to produce different sound levels for the same note by varying motor speeds (Fig. 4I and movie S4). When the finger is actuated at decreasing motor speeds (about 400°, 50°, and 25°/s) to press a piano key, the resulting maximum audio levels decrease to −10, −15, and −19 dBFS (decibels relative to full scale), respectively. The term dBFS measures the sound intensity, and a higher dBFS value indicates a "louder" sound (detailed in Materials and Methods). Spectrum analysis confirms that the pitches of the three produced sounds are not distorted by the varied motor speeds, with all frequencies centered around 512 Hz (Fig. 4J). In addition, a higher motor speed reduces the time required to generate the sound, which is consistent with the sound production principle of the piano (*55*).

Playing piano music with human-like dexterity

Having demonstrated the robotic hand's skills of piano playing, we further evaluate its ability to play musical pieces. This step is crucial in bridging the gap between isolated technical capabilities and the complex performance required for real-world applications. To this end, we select two contrasting pieces of music: "Always with me" and "Jasmine flower." These pieces have different musical styles, with the former being a lyrical emotive piece (across two octaves; Fig. 5A) and the latter being a lively technical piece (across three octaves; fig. S17).

For the performance of "Always with me," we control the anthropomorphic robotic hand to play all notes without resorting to whole-hand movements (fig. S18 and movie S5). The spectral analysis demonstrates that the robotic hand can play all notes with 100% accuracy, suggesting a high degree of precision in both timing and key selection (Fig. 5B). To evaluate the musical rhythm, we use the musical instrument digital interface (MIDI) signal for quantitative analysis (detailed in Materials and Methods). We compare the MIDI signals of the robotic hand against those of a human player and the standard notation (Fig. 5C). First, the time intervals of played consecutive short notes are slightly longer than those of the standard notation due to the frequent configuration change (i.e., flexion-extension and abduction-adduction) of the same finger. Second, some notes are played earlier because these notes are played by the thumb without tendon transmission. Third, the note end times for both the robotic hand and human player occur earlier than the standard notation because they both require sufficient response time to regulate the finger configurations.

The playing of "Jasmine flower" introduces more challenges for our robotic hand due to its lively tempo and intricate finger movement. It requires the robotic hand to use coordinated whole-hand translation enabled by the moving platform (maximum translation distance of 141 mm and maximum speed of 313 mm/s; see Fig. 5D). This approach is necessary to cover the wider range of notes and accommodate the frequent finger configuration changes demanded by the piece (detailed in Materials and Methods). Despite these increased challenges, the robotic hand demonstrates remarkable dexterity, playing all notes in time with 100% accuracy (see movie S6). The ability to reproduce musical pieces across contrasting styles highlights the manipulation dexterity and versatility of the robotic hand. This capability spans from delicate operations requiring fine motion control to more dynamic tasks necessitating rapid coordinated movements, demonstrating the potential for a wide range of real-world applications.

Dexterous grasping and manipulation

To illustrate the versatility of the anthropomorphic robotic hand, we conduct a series of grasping tests, primarily including power grasps and pinch grasps (movie S7). We show an example of how finger abduction assists in power grasping for ball-like objects (Fig. 6A). The abduction of the index and little fingers enables the robotic hand to apply closure forces around the baseball (about 82 mm by 82 mm by 82 mm), achieving a secure enveloping power grasp. Without finger abduction, the baseball is easily squeezed out of the hand. The compliance of the fingers allows the robotic hand to grasp a large wooden cube (about 130 mm by 130 mm by 130 mm) with holes of various shapes on its surface (Fig. 6B), as the fingers adapt to the contours of the holes. This finger compliance is particularly important for environmental and human interaction (Fig. 6C). Further, our robotic hand can grasp a flat plush toy (about 115 mm by 60 mm by 125 mm) from the desk surface (Fig. 6D), with the fingers passively adducting to conform to the desk constraints. In a pick-and-place task (Fig. 6E), five smaller objects of different shapes and sizes (a clamp, a table tennis ball, a sector column, a pine cone, and a massage ball; all with a maximum dimension of less than 55 mm) are successfully handled using pinch grasps. As demonstrated by test results on five ball-like objects, the inherent compliance of the robotic hand allows it to tolerate certain degrees of positional errors (table S2). In a cylinder grasping test, the measured maximum grasping force is 14.6 ± 2.9 N (see fig. S11 for detailed experimental setups). Details of all the experimental setups are provided in Materials and Methods.

We lastly conduct tests to evaluate the manipulation capabilities of our developed robotic hand. The experimental results demonstrate that our robotic hand can continuously rotate a knob (diameter, 36 mm) through cyclic motions including thumb opposition-reposition, finger flexion-extension, and finger abduction-adduction (Fig. 6F, movie S8, and table S3). The robotic hand can also perform in-hand manipulation of Baoding balls (diameter, 40 mm) through thumb opposition-reposition and the sequential flexion-extension of the fingers (Fig. 6G, movie S9, and table S4). Moreover, despite unexpected disturbances, it remains robust in manipulating Baoding balls (movie S9), demonstrating the advantages of our rigid-soft hybrid

Downloaded from https://www.science.org at Shanghai Jiao Tong University on April 28, 2025

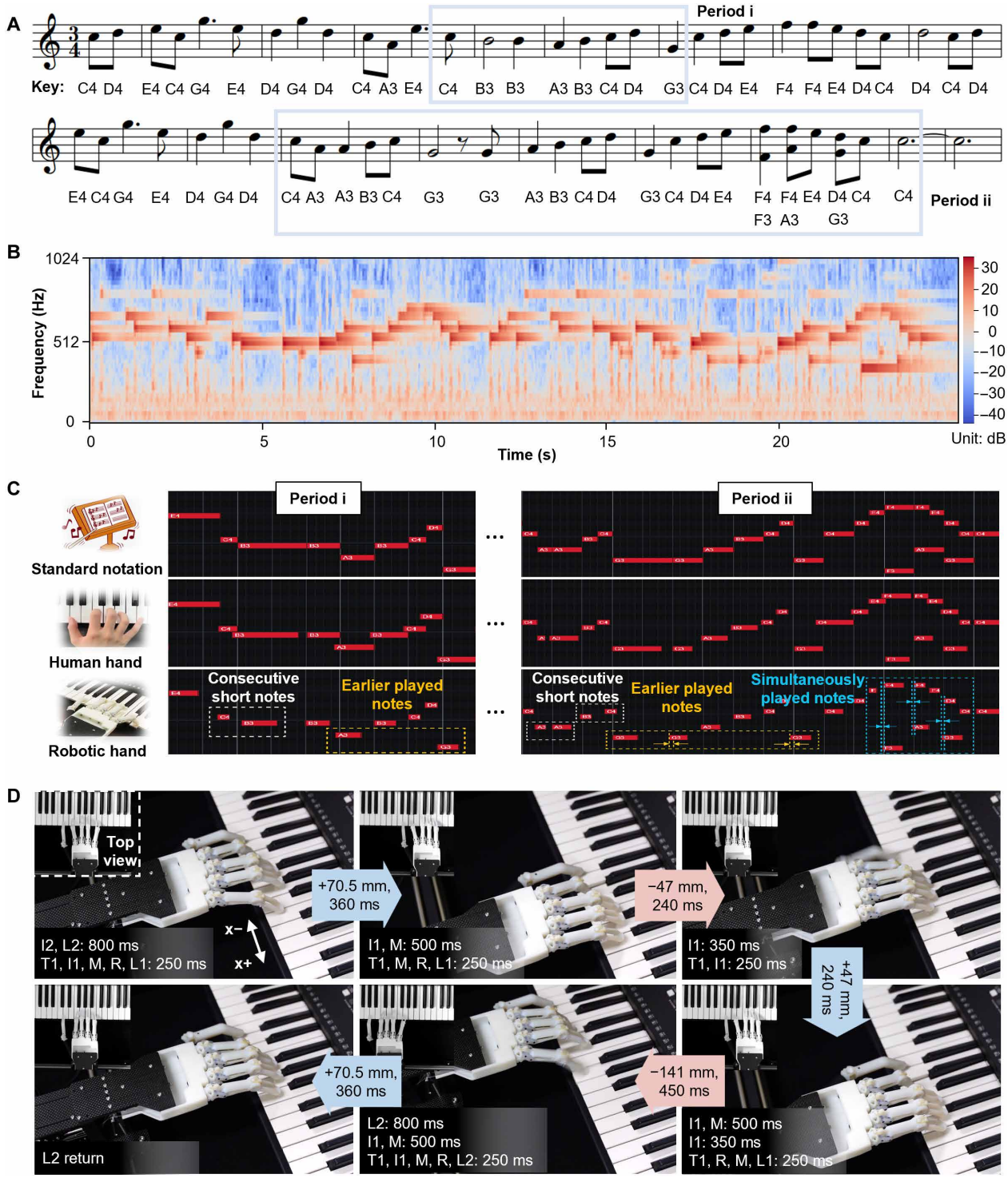

Fig. 5. Evaluation of the anthropomorphic robotic hand playing different music styles. (**A**) Illustration of the music score "Always with me." (**B**) The spectral analysis demonstrates the effectiveness of the robotic hand in performing the music "Always with me." (**C**) MIDI signal comparisons of the music played by the robotic hand, the human hand, and the standard notation. The horizontal axis, vertical axis, and red blocks indicate time variation, note variation, and note duration, respectively. The results demonstrate good agreement between them with only slight differences. (**D**) Demonstration of the robotic hand performing the music "Jasmine flower." In this process, the robotic hand cooperates with a moving platform. The hand movements (specific finger poses and execution times) and uniaxial platform translations (stroke and execution time) are coordinated.

Downloaded from https://www.science.org at Shanghai Jiao Tong University on April 28, 2025

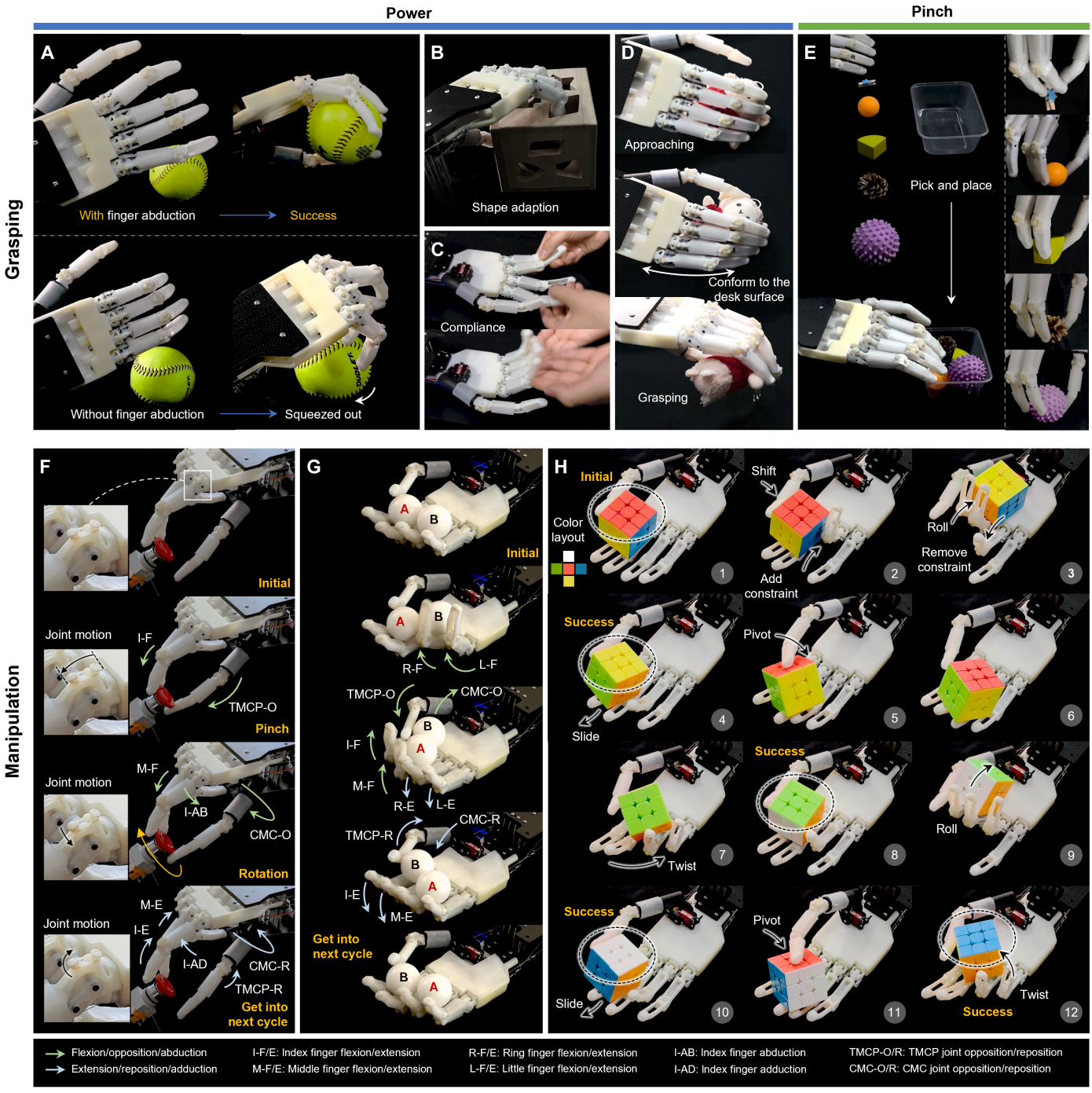

Fig. 6. Grasping and manipulation testing. (**A**) Comparison of grasping a baseball with and without finger abduction. The abduction of the index and little fingers enables the robotic hand to apply a pronounced closure force around the baseball, showing a secure enveloping power grasp. Without finger abduction, the baseball is easily squeezed out of the robotic hand. (**B**) A wooden cube with holes of various shapes on its surface is power grasped. The fingers adapt to the contours of the holes. (**C**) Demonstration of the robotic hand's compliance under external force. (**D**) A flat plush toy is power grasped from the desk surface. The fingers conform to the constraints of the desk surface. (**E**) Five objects with different shapes and sizes are pinch grasped in a pick-and-place task. (**F**) Demonstration of continuous knob rotation with cyclic finger motions. The knob has a diameter of 36 mm. (**G**) In-hand manipulation of the Baoding ball. Two balls are continuously rotated within the robotic hand through contact with different parts of the palm and fingers. This is achieved by the cyclic motions of five digits, including the opposition-reposition of the thumb and the sequential flexion-extension of the fingers. (**H**) In-hand manipulation of continuous turning different surfaces of a Rubik's cube through coordinated finger motions. The Rubik's cube has an edge length of 55 mm. The task aims to turn all adjacent surfaces of the red surface upward. The adjacent surfaces are colored yellow, green, white, and blue, respectively.

Downloaded from https://www.science.org at Shanghai Jiao Tong University on April 28, 2025

design for uncertain conditions. Figure 6H and movie S10 further show that the robotic hand can continuously turn a Rubik's cube (edge length, 55 mm) with programmable finger gaits (table S5). Notably, in all three manipulation tasks, the compliance of the fingers is indispensable, as it provides "soft" constraints and guidance to mitigate contact uncertainty, which is different from previous works (*50*, *56*, *57*). The details of all experimental setups are provided in Materials and Methods.

DISCUSSION

Despite decades of development, achieving human-like dexterity and adaptivity in robotic hands remains a significant challenge due to the high mechanical complexity required. Inspired by the coordinated interplay between rigid and soft structures in human hands and its role in achieving various functions, we hypothesized that mimicking this natural balance could address the challenge. Here, we present a biomimetic rigid-soft finger design that features regular-shaped skeletons, strategically deployed flexible ligaments, and elastic tendon actuation, preserving crucial kinematic and mechanical principles in a highly integrated form. As a result, the biomimetic finger can generate multi-df motions, including abduction-adduction and circumduction, closely mimicking a human-like workspace. This design remains resilient and compliant to external forces during long-term stable operations. Compared to existing works (table S6), our development achieves a more desirable integration of controllable active mobility and passive adaptivity, making our designed fingers well suited for dexterous manipulation and interaction.

Building upon this biomimetic finger design, our anthropomorphic robotic hand exhibits high dexterity and functionality when compared to current robotic hands (fig. S19 and table S7). It achieves active multi-df movements and passive flexibility with fewer control inputs, exemplifying the balance between functionality and simplicity. By relying primarily on embodied high mobility and adaptivity, our anthropomorphic robotic hand can master various piano playing skills, from coordinated wide-range keyboard striking to smooth adaptive keyboard interaction. These results demonstrate its versatility in handling complex manipulation such as different styles of music, opening possibilities for robotic hands in delicate tasks.

Beyond piano playing tasks, the biomimetic rigid-soft hybrid design has demonstrated effectiveness in general-purpose tasks. The high mobility enables effective power and pinch grasps, as well as complex in-hand manipulations. In addition, finger compliance reduces the control complexity and enhances the adaptability of the robotic hand in various applications. These features make the design suitable for a wide range of real-world tasks, bridging the gap from specialized to general applications.

To further enhance the finger dexterity and functionality, future work will focus on increasing the active df across multiphalangeal designs, improving multidirectional thumb mobility, and miniaturizing the actuation system for more compact implementations. Advancements in durable-material fabrication techniques, tendon tensioning mechanisms, and lubrication methods will potentially address the current issues related to the long-term reliability of our development. Studies on finger dimension size scales and optimized printing parameters can establish principles for rapid design iteration. Integrating fingers with advanced tactile sensing technologies (*58*), such as piezoelectric, capacitive, and camera-based, will enable closed loop control for more precise manipulation. Adaptive algorithms based on machine learning approaches (*59*) can better use the robotic hand's inherent compliance for robust operation. These enhancements will open opportunities for various applications, such as prosthetics, humanoid robots, and human-robot collaboration.

MATERIALS AND METHODS

Fabrication and assembly of the finger

We three-dimensionally print the finger skeletons using the resin material (VeroWhite, Stratasys Ltd.). We print the ligament shafts using nylon material (PA12, Yisheng Inc.) through fused deposition modeling. The ligaments of the MCP joint, which are made from selected Dragon Skin 30 (Smooth-On Inc.), are fabricated by molding. The tendon material and the ligament material of the IP joint are all high strength polyethylene (no. 8, Yun-shang Piao Inc.). The assembly steps for the finger are as follows. Insert and fix the ligament shafts into the holes on the corresponding skeletons, ensuring equal protrusion lengths. Apply the lubricant (no. 2, Kunlun Inc.) to the joint surfaces for lubrication. Mount the ligaments onto the shafts and apply a small amount of adhesive (Sil-Poxy, Smooth-On Inc.) to prevent ligament detachment during finger motion. Thread the polyethylene wire through the holes on the distal linkage and proximal linkage to form a closed-loop IP ligament. Hang an extensor on the back of the IP joint. Attach a polyethylene wire as the flexion tendon through the corresponding channels of the distal linkage, proximal linkage, and base. Attach another polyethylene wire as the abduction tendon through the corresponding channels of the proximal linkage and base. Hook orthodontic elastic strings [$^1/_8$, 3.5 oz. (99.2233 g); Ormco Inc.] as the joint extensors. In addition, apply lubricating grease to the joint surfaces and tendon channels to reduce friction and enhance smooth motion.

Assembly of the anthropomorphic robotic hand

Connect the thumb base to the thumb proximal (TP) linkage, forming the CMC joint. Mount the micro servomotor on the thumb base, with the servomotor's output shaft connected to the TP linkage to directly actuate the CMC joint. Install an additional bearing-supported shaft, aligned with the servomotor's output shaft, to ensure rotational stability at the CMC joint. Connect the TP linkage to the thumb distal (TD) linkage, forming the TMCP joint. Attach a tendon through the channels on the TP and TD linkages to actuate the TMCP joint. Print a palm structure with a size similar to the human hand (using VeroWhite, Stratasys Ltd.). Install four biomimetic rigid-soft robotic fingers on the palm and attach tendons with springs for actuation.

Experimental setups of the servomotors

The servomotors used in the experiment are of model STS3032 (Feetech Inc.). We use the software FD1.9.8.3 to control the servomotor, in which the rotation angle (360°) of the servomotor is mapped into 4096 steps. By inputting the required step value into the software, the servomotor can precisely rotate to the corresponding angle. To ensure consistent experimental conditions, we use the middle position calibration (MPC) function to reset the zero angle of the servomotor to the same position before each experiment. Specifically, we turn off the torque output function of the servomotor that prevents external force from changing the position of the servomotor and then manually rotate the servomotor to make the tendon in a pretense state, thus using the MPC function to complete the zero-angle setting. In the software, the sampling frequency is set to 20 Hz.

Downloaded from https://www.science.org at Shanghai Jiao Tong University on April 28, 2025

Control of the tendon displacement

In the performance characterization of the finger, we set the pulley radius $r_{pulley} = 12.5$ mm; therefore, the tendon displacement can be calculated by $l_{tendon} = r_{pulley} \times \pi/180$ mm $= 0.218$ mm. To acquire high accuracy of measurement, we select the angular speed of the servomotor as $\omega = 50$ step/s $= 50 \times 360/4096 = 4.39°$/s. The corresponding linear velocity of the tendon is derived by $v_{tendon} = r_{pulley} \times \omega \times \pi/180 = 0.96$ mm/s. This speed setting is used in most experiments. An exception is the durability test, where the angular speed of the servomotor is set to 439°/s to be as close as possible to the actual piano playing applications.

Setups for measuring dynamic properties

In the bandwidth measurement, we set the finger to perform repeated flexion-extension or abduction-adduction motion, with one round trip counted as a cycle (motion range of 90° and 30° for flexion-extension and abduction-adduction, respectively, at the MCP joint for measurement). The initial frequency is set to 0.5 Hz, corresponding to a cycle time of 2 s. Simultaneously, we use a visual tracking system to measure the finger's flexion or abduction angle. After completing 5 cycles, the cycle time is reduced, and the corresponding frequency gradually increases. The cycle time is continuously decreased, and the above process is repeated. The frequency at which the flexion or abduction angle reaches ~70% of the initial angle is identified as the bandwidth. For the flexion-extension motion, the cycle time decreases from 2 s (0.5 Hz) to 0.4 s (2.5 Hz). For the abduction-adduction motion, the cycle time decreases from 2 s (0.5 Hz) to 0.25 s (4 Hz). In the response time measurement, we set the finger to perform repeated flexion-extension or abduction-adduction motion. The time interval between the end time of the initial position and the start time of the next position is set to 1 s. Simultaneously, we use a visual tracking system to measure the finger motion and record the actual time consumed. The actual time minus 1 s is calculated as the response time.

Setups for the piano playing experiments

We use an electronic piano (PSR-E373, Yamaha Inc.) for the experiments. The anthropomorphic robotic hand is positioned with its fingertips 5 mm above the piano keyboard. In the initial position, the fingers are fully extended without abduction or adduction, while the TMCP joint is adducted and the CMC joint is fully extended. The spacing between adjacent fingers matches the width of a white key, and the span between the thumb and index finger covers two white keys. This configuration allows the anthropomorphic robotic hand to access a six-note interval, with the thumb and other fingers labeled as T1, I1, M1, R1, and L1, respectively.

Finite element analysis

The deformation behavior of the lateral elastic ligaments during flexion of the MCP joint is evaluated using the commercial finite element software Abaqus (SIMULIA, Providence, RI). The analysis uses 10-node quadratic tetrahedral elements to ensure precise stress and strain calculations. Quasi-static simulations are performed using the Abaqus/Standard solver, and mesh refinement is applied to improve computational accuracy. The simulation consists of two steps. First, the ligaments are prestretched to match the distance between the anchors. Then, the MCP joint flexes from 0° to 90°. The maximum local strain in the above two steps is determined by identifying the peak value of the maximum principal strain across all elements.

Audio analyses

We use Mel spectrum to analyze the frequency feature of audio: $f =$ FFT (fast Fourier transform; audio) and $m = 2595 \lg(1 + f/700)$. The parameter f is obtained by the FFT, and parameter m is the Mel spectrum. These processes are performed in the Python Librosa library function for visualization. We use the Adobe Premiere Pro software to evaluate the sound levels. The MIDI signals convey rich musical information such as notes, time points, and note durations. We use the software (Cubase 10 Pro, Steinberg Inc.) to record the MIDI signals during the piano playing processes.

Experimental setups of grasping and manipulation tests

We use the anthropomorphic robotic hand solely for conducting experiments, without incorporating the moving platform. The finger linkages and palm are equipped with soft elastomeric pads or sockets, which are made of silicone Dragon Skin 10 (Smooth-On Inc.). During grasping experiments, the arm of the robotic hand is held by an assistant. For manipulation experiments, the robotic hand remains fixed in place.

Supplementary Materials

The PDF file includes:

Supplementary Text S1 to S6
Figs. S1 to S19
Tables S1 to S7
Legends for movies S1 to S10

Other Supplementary Material for this manuscript includes the following:

Movies S1 to S10

REFERENCES AND NOTES

1. C. Piazza, G. Grioli, M. G. Catalano, A. Bicchi, A century of robotic hands. *Annu. Rev. Control Robot. Auton. Syst.* **2**, 1–32 (2019).
2. C.-H. Xiong, W.-R. Chen, B.-Y. Sun, M.-J. Liu, S.-G. Yue, W.-B. Chen, Design and implementation of an anthropomorphic hand for replicating human grasping functions. *IEEE Trans. Robot.* **32**, 652–671 (2016).
3. A. Billard, D. Kragic, Trends and challenges in robot manipulation. *Science* **364**, eaat8414 (2019).
4. U. Kim, D. Jung, H. Jeong, J. Park, H.-M. Jung, J. Cheong, H. R. Choi, H. Do, C. Park, Integrated linkage-driven dexterous anthropomorphic robotic hand. *Nat. Commun.* **12**, 7177 (2021).
5. R. F. Shepherd, F. Ilievski, W. Choi, S. A. Morin, A. A. Stokes, A. D. Mazzeo, X. Chen, M. Wang, G. M. Whitesides, Multigait soft robot. *Proc. Natl. Acad. Sci. U.S.A.* **108**, 20400–20403 (2011).
6. D. Rus, M. T. Tolley, Design, fabrication and control of soft robots. *Nature* **521**, 467–475 (2015).
7. C. Laschi, B. Mazzolai, M. Cianchetti, Soft robotics: Technologies and systems pushing the boundaries of robot abilities. *Sci. Robot.* **1**, eaah3690 (2016).
8. G. Gu, J. Zhu, L. Zhu, X. Zhu, A survey on dielectric elastomer actuators for soft robots. *Bioinspir. Biomim.* **12**, 011003 (2017).
9. R. Baines, S. K. Patiballa, J. Booth, L. Ramirez, T. Sipple, A. Garcia, F. Fish, R. Kramer-Bottiglio, Multi-environment robotic transitions through adaptive morphogenesis. *Nature* **610**, 283–289 (2022).
10. G. Li, X. Chen, F. Zhou, Y. Liang, Y. Xiao, X. Cao, Z. Zhang, M. Zhang, B. Wu, S. Yin, Y. Xu, H. Fan, Z. Chen, W. Song, W. Yang, B. Pan, J. Hou, W. Zou, S. He, X. Yang, G. Mao, Z. Jia, H. Zhou, T. Li, S. Qu, Z. Xu, Z. Huang, Y. Luo, T. Xie, J. Gu, S. Zhu, W. Yang, Self-powered soft robot in the Mariana Trench. *Nature* **591**, 66–71 (2021).
11. S. Li, D. M. Vogt, D. Rus, R. J. Wood, Fluid-driven origami-inspired artificial muscles. *Proc. Natl. Acad. Sci. U.S.A.* **114**, 13132–13137 (2017).
12. M. G. Catalano, G. Grioli, E. Farnioli, A. Serio, C. Piazza, A. Bicchi, Adaptive synergies for the design and control of the Pisa/IIT SoftHand. *Int. J. Robot. Res.* **33**, 768–782 (2014).
13. A. M. Dollar, R. D. Howe, The highly adaptive SDM Hand: Design and performance evaluation. *Int. J. Robot. Res.* **29**, 585–597 (2010).
14. R. Deimel, O. Brock, A novel type of compliant and underactuated robotic hand for dexterous grasping. *Int. J. Robot. Res.* **35**, 161–185 (2016).
15. H. Zhao, K. O'Brien, S. Li, R. F. Shepherd, Optoelectronically innervated soft prosthetic hand via stretchable optical waveguides. *Sci. Robot.* **1**, eaai7529 (2016).

Downloaded from https://www.science.org at Shanghai Jiao Tong University on April 28, 2025

16. J. Zhou, X. Chen, U. Chang, J. Lu, C. C. Y. Leung, Y. Chen, Y. Hu, Z. Wang, A soft-robotic approach to anthropomorphic robotic hand dexterity. *IEEE Access* **7**, 101483–101495 (2019).
17. G. Gu, N. Zhang, H. Xu, S. Lin, Y. Yu, G. Chai, L. Ge, H. Yang, Q. Shao, X. Sheng, X. Zhu, X. Zhao, A soft neuroprosthetic hand providing simultaneous myoelectric control and tactile feedback. *Nat. Biomed. Eng.* **7**, 589–598 (2023).
18. K. C. Galloway, K. P. Becker, B. Phillips, J. Kirby, S. Licht, D. Tchernov, R. J. Wood, D. F. Gruber, Soft robotic grippers for biological sampling on deep reefs. *Soft Robot.* **3**, 23–33 (2016).
19. A. Mohammadi, J. Lavranos, H. Zhou, R. Mutlu, G. Alici, Y. Tan, P. Choong, D. Oetomo, A practical 3D-printed soft robotic prosthetic hand with multi-articulating capabilities. *PLOS ONE* **15**, e0232766 (2020).
20. F. Connolly, C. J. Walsh, K. Bertoldi, Automatic design of fiber-reinforced soft actuators for trajectory matching. *Proc. Natl. Acad. Sci. U.S.A.* **114**, 51–56 (2017).
21. Y. Li, Y. Chen, Y. Yang, Y. Wei, Passive particle jamming and its stiffening of soft robotic grippers. *IEEE Trans. Robot.* **33**, 446–455 (2017).
22. Y.-F. Zhang, N. Zhang, H. Hingorani, N. Ding, D. Wang, C. Yuan, B. Zhang, G. Gu, Q. Ge, Fast-response, stiffness-tunable soft actuator by hybrid multimaterial 3D printing. *Adv. Funct. Mater.* **29**, 1806698 (2019).
23. S. Puhlman, J. Harris, O. Brock, RBO Hand 3: A platform for soft dexterous manipulation. *IEEE Trans. Robot.* **38**, 3434–3449 (2022).
24. S. Abondance, C. B. Teeple, R. J. Wood, A dexterous soft robotic hand for delicate in-hand manipulation. *IEEE Robot. Autom. Lett.* **5**, 5502–5509 (2020).
25. C. De Pascali, G. A. Naselli, S. Palagi, R. B. N. Scharff, B. Mazzolai, 3D-printed biomimetic artificial muscles using soft actuators that contract and elongate. *Sci. Robot.* **7**, eabn4155 (2022).
26. C. B. Teeple, T. N. Koutros, M. A. Graule, R. J. Wood, Multi-segment soft robotic fingers enable robust precision grasping. *Int. J. Robot. Res.* **39**, 1647–1667 (2020).
27. J. Shintake, V. Cacucciolo, D. Floreano, H. Shea, Soft robotic grippers. *Adv. Mater.* **30**, 1707035 (2018).
28. Z. Xu, E. Todorov, "Design of a highly biomimetic anthropomorphic robotic hand towards artificial limb regeneration" in *2016 IEEE International Conference on Robotics and Automation (ICRA)* (IEEE, 2016), pp. 3485–3492.
29. N. Zhang, L. Ge, H. Xu, X. Zhu, G. Gu, 3D printed, modularized rigid-flexible integrated soft finger actuators for anthropomorphic hands. *Sens. Actuators A Phys.* **312**, 112090 (2020).
30. Y. Zhu, G. Wei, L. Ren, Z. Luo, J. Shang, An anthropomorphic robotic finger with innate human-finger-like biomechanical advantages part I: Design, ligamentous joint, and extensor mechanism. *IEEE Trans. Robot.* **39**, 485–504 (2022).
31. T. J. K. Buchner, S. Rogler, S. Weirich, Y. Armati, B. G. Cangan, J. Ramos, S. T. Twiddy, D. M. Marini, A. Weber, D. Chen, G. Ellson, J. Jacob, W. Zengerle, D. Katalichenko, C. Keny, W. Matusik, R. K. Katzschmann, Vision-controlled jetting for composite systems and robots. *Nature* **623**, 522–530 (2023).
32. H. Lee, J. Park, B. B. Kang, K.-J. Cho, Single-step 3D printing of bio-inspired printable joints applied to a prosthetic hand. *3D Print. Addit. Manuf.* **10**, 917–929 (2022).
33. D. Wang, J. Wang, Z. Shen, C. Jiang, J. Zou, L. Dong, N. X. Fang, G. Gu, Soft actuators and robots enabled by additive manufacturing. *Annu. Rev. Control Robot. Auton. Syst.* **6**, 31–63 (2023).
34. S. D. Gollob, J. Poss, G. Memoli, E. T. Roche, A multi-material, anthropomorphic metacarpophalangeal joint with abduction and adduction actuated by soft artificial muscles. *IEEE Robot. Autom. Lett.* **7**, 5882–5887 (2022).
35. W. Ruotolo, D. Brouwer, M. R. Cutkosky, From grasping to manipulation with gecko-inspired adhesives on a multifinger gripper. *Sci. Robot.* **6**, eabi9773 (2021).
36. P. Zhou, N. Zhang, G. Gu, A biomimetic soft-rigid hybrid finger with autonomous lateral stiffness enhancement. *Adv. Intell. Syst.* **4**, 2200170 (2022).
37. K. Gilday, J. Hughes, F. Iida, Wrist-driven passive grasping: Interaction-based trajectory adaption with a compliant anthropomorphic hand. *Bioinspir. Biomim.* **16**, 026024 (2021).
38. K. W. O'Brien, A. Xu, D. J. Levine, C. A. Aubin, H.-J. Yang, M. F. Xiao, L. W. Wiesner, R. F. Shepherd, Elastomeric passive transmission for autonomous force-velocity adaptation applied to 3D-printed prosthetics. *Sci. Robot.* **3**, eaau5543 (2018).
39. J. A. E. Hughes, P. Maiolino, F. Iida, An anthropomorphic soft skeleton hand exploiting conditional models for piano playing. *Sci. Robot.* **3**, eaau3098 (2018).
40. Y.-F. Li, C.-Y. Lai, "Intelligent algorithm for music playing robot—Applied to the anthropomorphic piano robot control" in *2014 IEEE 23rd International Symposium on Industrial Electronics (ISIE)* (IEEE, 2014), pp. 1538–1543.
41. D. Zhang, J. Lei, B. Li, D. Lau, C. Cameron, "Design and analysis of a piano playing robot" in *2009 International Conference on Information and Automation* (IEEE, 2009), pp. 757–761.
42. B. Mosadegh, P. Polygerinos, C. Keplinger, S. Wennstedt, R. F. Shepherd, U. Gupta, J. Shim, K. Bertoldi, C. J. Walsh, G. M. Whitesides, Pneumatic networks for soft robotics that actuate rapidly. *Adv. Funct. Mater.* **24**, 2163–2170 (2014).
43. C. Borst, M. Fischer, S. Haidacher, H. Liu, G. Hirzinger, "DLR hand II: Experiments and experience with an anthropomorphic hand" in *2003 IEEE International Conference on Robotics and Automation* (IEEE, 2003), pp. 702–707.
44. S. Hoang, K. Karydis, P. Brisk, W. H. Grover, A pneumatic random-access memory for controlling soft robots. *PLOS ONE* **16**, e0254524 (2021).
45. M. Mahato, R. Tabassian, V. H. Nguyen, S. Oh, S. Nam, W.-J. Hwang, I.-K. Oh, CTF-based soft touch actuator for playing electronic piano. *Nat. Commun.* **11**, 5358 (2020).
46. D. A. Neumann, in *Kinesiology of the Musculoskeletal System* (Mosby, 2002), pp. 25–40.
47. G. Palli, C. Melchiorri, G. Vassura, U. Scarcia, L. Moriello, G. Berselli, A. Cavallo, G. De Maria, C. Natale, S. Pirozzi, C. May, F. Ficuciello, B. Siciliano, The DEXMART hand: Mechatronic design and experimental evaluation of synergy-based control for human-like grasping. *Int. J. Robot. Res.* **33**, 799–824 (2014).
48. D.-H. Lee, J.-H. Park, S.-W. Park, M.-H. Baeg, J.-H. Bae, KITECH-Hand: A highly dexterous and modularized robotic hand. *IEEE/ASME Trans. Mech.* **22**, 876–887 (2017).
49. M. Laffranchi, N. Boccardo, S. Traverso, L. Lombardi, M. Canepa, A. Lince, M. Semprini, J. A. Saglia, A. Naceri, R. Sacchetti, E. Gruppioni, L. De Michieli, The Hannes hand prosthesis replicates the key biological properties of the human hand. *Sci. Robot.* **5**, eabb0467 (2020).
50. M. Grebenstein, M. Chalon, W. Friedl, S. Haddadin, T. Wimböck, G. Hirzinger, R. Siegwart, The hand of the DLR hand arm system: Designed for interaction. *Int. J. Robot. Res.* **31**, 1531–1555 (2012).
51. B. Hirt, H. Seyhan, M. Wagner, R. Zumhasch, in *Hand and Wrist Anatomy and Biomechanics: A Comprehensive Guide* (Thieme, 2017), pp. 66–70.
52. R. J. Schultz, A. Storace, S. Krishnamurthy, Metacarpophalangeal joint motion and the role of the collateral ligaments. *Int. Orthop.* **11**, 149–155 (1987).
53. U. Jeong, K. Kim, S. H. Kim, H. Choi, B. D. Youn, K. J. Cho, Reliability analysis of a tendon-driven actuation for soft robots. *Int. J. Robot. Res.* **40**, 494–511 (2021).
54. J. J. Lister, R. A. Roberts, J. Shackelford, C. L. Rogers, An adaptive clinical test of temporal resolution. *Am. J. Audiol.* **15**, 133–140 (2007).
55. H. Suzuki, I. Nakamura, Acoustics of pianos. *Appl. Acoust.* **30**, 147–205 (1990).
56. O. M. Andrychowicz, B. Baker, M. Chociej, R. Jozefowicz, B. McGrew, J. Pachocki, A. Petron, M. Plappert, G. Powell, A. Ray, J. Schneider, S. Sidor, J. Tobin, P. Welinder, L. Weng, W. Zaremba, Learning dexterous in-hand manipulation. *Int. J. Robot. Res.* **39**, 3–20 (2020).
57. W. G. Bircher, A. S. Morgan, A. M. Dollar, Complex manipulation with a simple robotic hand through contact breaking and caging. *Sci. Robot.* **6**, eabd2666 (2021).
58. J. Qu, B. Mao, Z. Li, Y. Xu, K. Zhou, X. Cao, Q. Fan, M. Xu, B. Liang, H. Liu, X. Wang, Recent progress in advanced tactile sensing technologies for soft grippers. *Adv. Funct. Mater.* **33**, 2306249 (2023).
59. O. Kroemer, S. Niekum, G. Konidaris, A review of robot learning for manipulation: Challenges, representations, and algorithms. *J. Mach. Learn. Res.* **22**, 1395–1476 (2021).

Acknowledgments: We thank the support from the Xplorer Prize. We also thank J. Liu, J. Li, D. Yang, and Y. Dong for discussions and suggestions on the paper content and illustrations. **Funding:** This work was supported in part by the National Key R&D Program of China (grant no. 2024YFB4707504), the National Natural Science Foundation of China (grant nos. 52025057 and 52305029), the Science and Technology Commission of Shanghai Municipality (grant no. 24511103400), the China Postdoctoral Innovation Talents Support Program (grant no. BX20220204), and the China Postdoctoral Science Foundation (grant no. 2022 M722085).
Author contributions: N.Z., P.Z., X.Z., and G.G. conceived the idea. N.Z., P.Z., and X.Y. designed the study. N.Z., P.Z., and F.S. conducted the experiments. N.Z., F.S., P.Z., X.Y., J.R., T.H., L.D., and R.B. analyzed and interpreted the results. N.Z. wrote the original draft. D.W., G.G., and X.Z. reviewed and edited the writing. X.Z. and G.G. directed the project. **Competing interests:** The authors declare that they have no competing interests. **Data and materials availability:** All data needed to evaluate the conclusions in the paper are present in the paper and/or the Supplementary Materials.

Submitted 28 October 2024
Accepted 19 March 2025
Published 23 April 2025
10.1126/sciadv.adu2018

Downloaded from https://www.science.org at Shanghai Jiao Tong University on April 28, 2025